

PAPER View Article Online

# Synthesis and mechanical response of disordered colloidal micropillars†

Cite this: DOI: 10.1039/c3cp55422h

Daniel J. Strickland, <sup>a</sup> Lei Zhang, <sup>bc</sup> Yun-Ru Huang, <sup>b</sup> Daniel J. Magagnosc, <sup>a</sup> Daeyeon Lee\* <sup>b</sup> and Daniel S. Gianola\* <sup>a</sup>

We present a new approach for studying the uniaxial compressive behavior of colloidal micropillars as a function of the initial defect population, pillar and colloid dimension, and particle–particle interaction. Pillars composed of nanometer scale particles develop cracks during drying, while pillars composed of micron scale particles dry crack-free. We subject the free-standing pillars, with diameters of 580  $\mu$ m and 900  $\mu$ m, to uniaxial compression experiments using a custom-built micromechanical testing apparatus. In pillars with pre-existing cracks, compression activates the macroscopic defects, leading to fracture and stochastic mechanical response as a result of the flaw distribution. Pillars that dry crack-free fail by shear bands that initiate near the punch face. While macroscopically identical, pillar-to-pillar mechanical response varies significantly. We attribute the disparate response to varying structure and environmental conditions. To isolate the effects of environment, we performed controlled experiments over a range of relative humidity levels (<2% to >98% RH). The level of atmospheric humidity affects particle–particle cohesion and friction, resulting in dramatically different mechanical responses. We discuss the results in the context of underlying particle rearrangements leading to mesoscopic shear localization and examine comparisons with atomic disordered systems such as metallic glasses.

Received 24th December 2013, Accepted 11th April 2014

DOI: 10.1039/c3cp55422h

www.rsc.org/pccp

#### 1. Introduction

Model systems of bubbles, colloids, and grains have played crucial roles in guiding and confirming our understanding of atomic solids. Two well-known examples are the bubble raft experiments of Bragg and Nye, 1,2 which were a powerful tool in refining theories of defects in the mechanical behavior of metals, and the colloidal silica systems of Schall, Weitz, and Spaepen, which provided direct visualization of particle-scale rearrangements in sheared amorphous solids. Even though care must be taken when comparing the behavior of atomic systems to model analogs, model systems possess two experimental advantages in comparison to atomic systems in (1) the ability to resolve the real-space positions of individual particles and (2) the ability to alter particle-particle interactions.

In atomic solids, microscopic structure and dynamics are typically deduced from ensemble-averaged quantities obtained from scattering experiments.<sup>4</sup> Therefore, linking the macroscopic response of an atomic system to particle-scale events is a

formidable challenge. Model systems, however, allow for the determination of the positions of individual particles. For two-dimensional systems, a simple camera or optical microscope is often sufficient for collecting position information. Three-dimensional systems, which are often desirable for exploring bulk properties of solids, may require more complex techniques. In recent years, full structural determination of three-dimensional systems of colloids and grains has been achieved using techniques such as confocal microscopy, magnetic resonance imaging, and X-ray tomography.<sup>5–10</sup> When perturbed by external stimuli such as boundary displacements or magnetic fields, the macroscopic response of the system may be directly correlated with microscopic structure and dynamics. This particle-scale resolution is often critical in understanding the macroscopic system response.

In addition to full real-space structure determination, model systems also allow for the manipulation of particle-particle interactions. The parameters that are altered to change the interactions depend on the nature of the constituent particles and their environment. For example, in a suspension of colloidal poly(methyl methacrylate) (PMMA) particles, Yethiraj and van Blaaderen adjusted the repulsive interaction distance and bond directionality by altering the salt content and the strength of an external electric field, respectively. In systems of larger granular particles, the moisture content of the structure affects particle-particle cohesion and friction. Frye and Marone found that the surface chemistry of grains and the environmental

<sup>&</sup>lt;sup>a</sup> Department of Materials Science and Engineering, University of Pennsylvania, USA. E-mail: gianola@seas.upenn.edu

b Department of Chemical and Biomolecular Engineering, University of Pennsylvania, USA. E-mail: daeyeon@seas.upenn.edu

<sup>&</sup>lt;sup>c</sup> Department of Mechanical Engineering, University of Alaska Fairbanks, USA

<sup>†</sup> Electronic supplementary information (ESI) available. See DOI: 10.1039/c3cp55422h

humidity significantly affected the shear response of a confined granular system. <sup>12</sup> Taken as a whole, the nature of interparticle interactions can be tailored, resulting in a diverse set of applicable analog atomic materials.

In this article we present a new model system designed to provide insight into the plastic deformation of amorphous solids - solids that lack long-range translational symmetry. Plasticity in amorphous solids cannot be described by the well-defined structure and dynamics of the defects found in crystalline materials. 13 It is known that shear banding, or the concentration of plastic flow in a narrow band of material, is a common deformation mode in amorphous solids found with surprising ubiquity irrespective of the underlying characteristic (particle) length scale comprising the solid. For example, bulk metallic glasses (BMGs),<sup>14</sup> disordered nanoparticle assemblies,<sup>15</sup> amorphous bubble rafts, 16 and soils 17 are all known to exhibit shear bands. Shear banding is the result of local softening that promotes strongly heterogeneous deformation. Argon proposed the shear transformation zone (STZ), envisaged as a dilatory, shear-induced rearrangement of  $\sim 100$  particles, as the fundamental plastic mechanism responsible for local softening.<sup>18</sup> In atomic systems, STZ operation is believed to result in a longrange elastic strain field that promotes subsequent STZ operation and local softening owing to the dilatory nature of the event. At a critical level of softening, this local region becomes unstable, and macroscopic shear bands result. Falk and Langer extended Argon's STZ mechanism into a theory that successfully describes many responses observed in both amorphous atomic<sup>13,19</sup> and colloidal-granular systems.<sup>20</sup> However, direct observation of STZ operation in atomic systems remains challenging, although some recent experiments demonstrate remarkable progress in this endeavor.21 Even more challenging than imaging local atomic rearrangements is capturing the dynamics that occur between a local rearrangement and shear band propagation. Furthermore, recent experiments and theory suggest that the external dimensions of atomic glasses control the mode of plastic deformation, with submicron specimens behaving in a ductile-like fashion relative to their bulk counterparts. 22,23 Whether extrinsic or intrinsic effects govern this apparent transition is still a matter of debate; however, the plastic behavior would be expected to change when the length scales approach the STZ size. We believe that model systems have the potential to add fundamental insight to these problems.

In this work, we report on the preparation and uniaxial compression of colloidal micropillars with diameters of 580 and 900 µm. To the best of our knowledge, the small constituent colloid size in these micropillars makes them unique in comparison to other dry colloidal–granular systems reported in literature. The small colloid size results in a large ratio of the cohesive particle–particle force to the gravitational body force on each particle. A simple approximation of this ratio for a pair of 6 µm polystyrene spheres bound by a water bridge gives a value of  $\sim 10^4,^{24}$  [see calculation in ESI†], which is  $\sim 100\times$  the ratio found for millimeter scale grains. Therefore, the micropillars are able to withstand a significant bending moment without collapsing and can be made free-standing. Free-standing pillars allow for uniaxial compression experiments to be performed

without confining the pillar surfaces, allowing us to explore the effects of free surfaces on deformation behavior. We note that the confining pressure necessary in experiments on packings of larger granular particles, which is known to affect the strength, failure morphology, and dilatancy observed, <sup>26</sup> is not required in our experiments. The extent of free surface in the micropillar geometry is unique in comparison to other colloidal deformation experiments such as the indentation experiments of Rahmani, <sup>27</sup> the 3-D simple shear experiments of Chikkadi, <sup>6</sup> and the 2-D shear experiments of Keim. <sup>28</sup> While not studied exhaustively in this report, the micropillars may assist in elucidating the effect of free surfaces on shear band nucleation and the intrinsic strength of amorphous solids.

### 2. Methods

#### 2.1. Materials

Spherical SiO<sub>2</sub> particles with an average diameter of 85 nm (30–31 wt% suspension in isopropanol, particle sizes ranging between 70 nm and 100 nm) are generously provided by Nissan Chemical America Corporation. Spherical SiO<sub>2</sub> nanoparticles with an average diameter of 250 nm and a standard deviation <10% are purchased from Fiber Optic Center, Inc. Polystyrene (PS) spheres with diameters of 3.004  $\pm$  0.065  $\mu m$  (2.64% solid-latex) and 6.15  $\pm$  0.188  $\mu m$  (10% solids) are purchased from Polyscience, Inc. and Bangs Laboratories, Inc., respectively. Standard glass capillaries with inner diameter (ID) of 580  $\mu m$  and outer diameter (OD) of 1000  $\mu m$  are purchased from World Precision Instruments, Inc. Borosilicate glass capillaries with an ID of 900  $\mu m$  and an OD of 1000  $\mu m$  are purchased from Produstrial LLC.

#### 2.2. Micropillar fabrication

The as-purchased glass capillaries are cut into shorter pieces with a length of 4 cm using a glass cutter. The two ends of each capillary are polished using a polishing wheel and 6  $\mu m$  diamond-impregnated polymer film to make the cross-sectional region of the capillary flat and smooth. The polished capillaries are cleaned with isopropanol to remove the impurities introduced during the polishing process. The micropillar fabrication procedure is shown in Fig. 1. To prevent the adhesion of colloidal particles to the inner walls of capillaries during the drying process, the empty capillaries are silanized with octade-cyltrichlorosilane (OTS) in toluene to render the inner surface hydrophobic (Fig. 1a and b).

A 25 wt% 250 nm  ${\rm SiO_2}$  aqueous suspension is prepared for the micropillar fabrication. The as-received 85 nm  ${\rm SiO_2}$  and 6.15  ${\rm \mu m}$  PS suspensions are concentrated using a centrifuge at 1000 rpm for 10 min by removing a significant amount of the supernatant. The  ${\rm SiO_2}$  or PS colloidal particle suspension is subsequently injected into the capillaries using a disposable syringe. The open end of the syringe is fitted with a 304 stainless steel and polytetra-fluoroethylene (PTFE) dispensing needle and plastic tubing to help direct the suspension flow into the capillaries (Fig. 1c). The capillary filled with a suspension containing colloidal particles is placed horizontally at room temperature and allowed to dry.

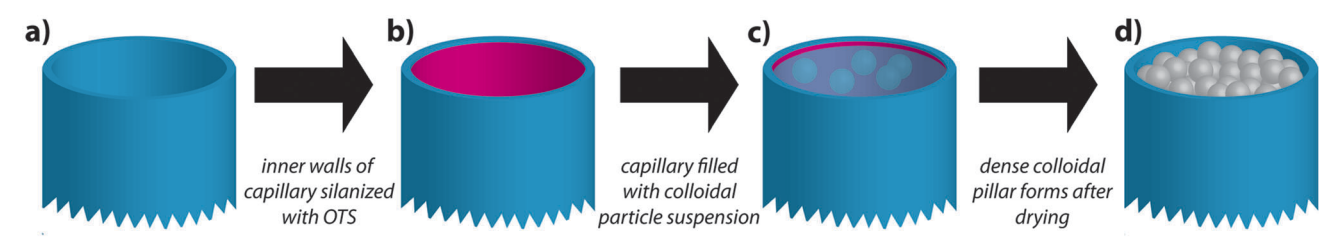


Fig. 1 Procedure for forming colloidal micropillars in capillary tube. (a) An empty capillary tube is first (b) silanized with OTS to make the inner surface hydrophobic. The capillary is (c) filled with a suspension containing colloidal particles. After drying, a (d) dense pillar remains. Note that pillars are filled (steps a-c) in the vertical position (as shown), while placed horizontally during drying (step d).

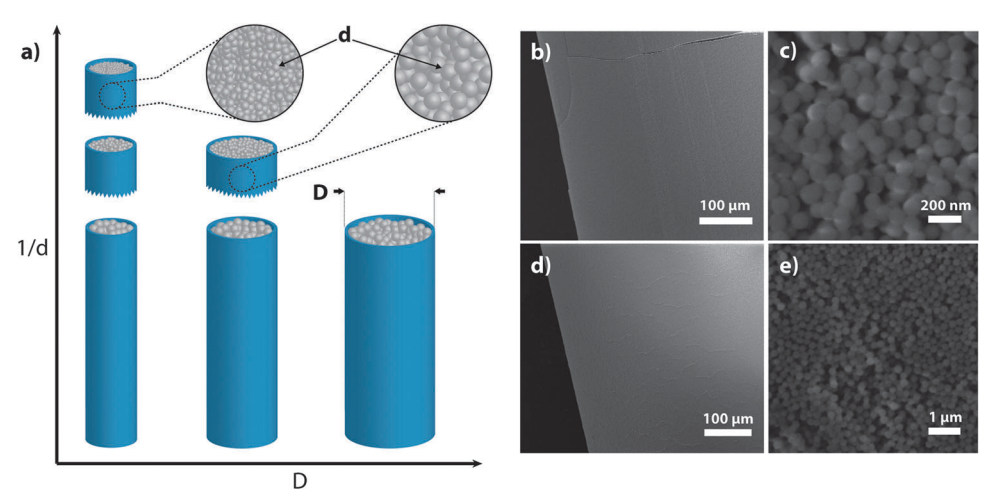


Fig. 2 (a) Both the capillary diameter, D, and the colloid diameter, d, may be varied. (b) A 580 μm pillar composed of (c) 85 nm SiO<sub>2</sub> particles and a (d) 580 um pillar composed of (e) 250 nm SiO<sub>2</sub> particles.

The drying process typically takes 3 days. After the water in the capillary has completely evaporated, a dense micropillar is formed toward one side of the capillary (Fig. 1d). The procedure for creating a free-standing pillar suitable for compression experiments from a confined pillar is described in Section 2.3.

While not systematically explored in this work, the structure of the micropillars may be varied by changing the capillary diameter, D, and the colloidal particle diameter, d (Fig. 2a). We find that pillars composed of small SiO2 particles develop cracks during drying (Fig. 3a and b), while pillars composed of 6.15 µm or a bidisperse mixture of 3 and 6.15 µm PS spheres (hereafter referred to as 3/6 µm) (Fig. 3c) do not. This result, presented as a map in Fig. 3d, is consistent with previous observations on the effect of colloid size on crack formation in drying colloidal thin-films.<sup>29,30</sup> Pillars composed of 6.15 µm PS show crystallization due to the small polydispersity. To avoid the crystallization of PS monodisperse particles, we prepare a bidisperse suspension by mixing the 3 µm PS suspension and 6.15 µm PS suspension with a volume ratio of 3.78.31 The amorphous structure is confirmed from SEM micrographs (see Fig. 4).

#### 2.3. Compression experiments

Uniaxial compression experiments are performed to probe the plastic response and fracture properties of the micropillars. Sample geometry is known to affect the deformation mode

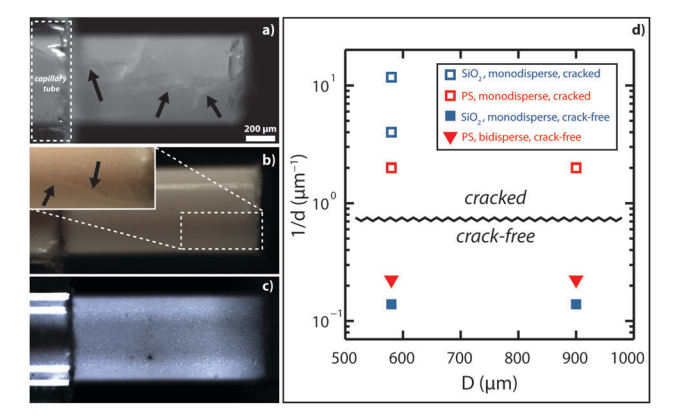


Fig. 3 580 μm diameter pillars composed of (a) 85 nm SiO<sub>2</sub> spheres, (b) 250 nm SiO<sub>2</sub> spheres, and (c) a mixture of 3 and 6 μm PS spheres. Black arrows indicate cracks that developed in the pillars during the drying process. Scale bar is the same for each frame. The inset in frame b shows a contrastenhanced region of pre-cracks. (d) Pillars composed of larger particles show no evidence of the cracking observed in the pillars composed of smaller particles. Pillars composed of SiO<sub>2</sub> particles are indicated by blue markers. Pillars composed of PS particles are indicated by red markers. Squares denote pillars composed of monodisperse particles and triangles denote pillars composed of bidisperse particles. Open symbols indicated pillars that form with cracks and filled symbols indicate pillars that form crack-free.

observed in compression experiments.<sup>32</sup> To promote shearing, as opposed to buckling or barreling, the aspect ratio of the

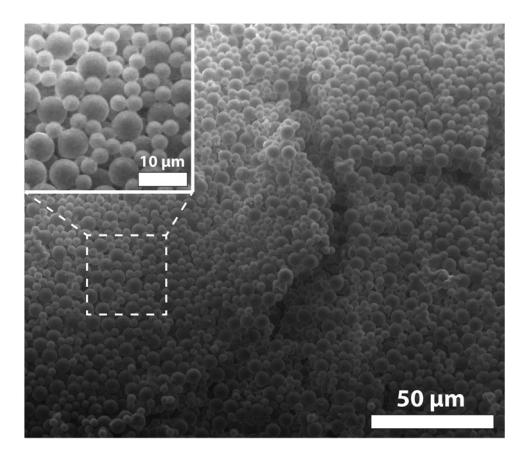


Fig. 4 SEM micrograph of the surface of a deformed 900  $\mu$ m diameter pillar composed of 3 and 6  $\mu$ m polystyrene spheres.

micropillars  $(l_0/D)$ , where  $l_0$  is the exposed pillar length and D is the pillar diameter) is maintained at values between  $\sim 2.2$  and  $\sim$  2.6. The small size and fragility of the micropillars make preparing and securing samples for compression experiments non-trivial. To assist in this process, a custom grip has been designed (see Fig. 5a). A polished steel wire is inserted into the capillary and brought into contact with the pillar. The smooth wire face ensures uniform contact between the wire and pillar and aids in preserving the initial pillar structure. The length of the wire is adjusted so that several centimeters remain exposed from the capillary after contact with the pillar is made. The capillary/wire assembly is secured to the grip using a clamp (see Fig. 5b) and the exposed face of the wire is brought into contact with a finely-threaded drive screw. Driving the screw pushes the pillar through the capillary and allows for precise control of the length of the exposed pillar that emerges from the opposite end. The wire also serves to backstop the pillar during the compression experiment. The jammed configuration of particles within the capillaries provides a relatively rigid constraint during compression testing of the exposed pillar.

Once the capillary is secured to the grip, the grip is attached to a load cell (GSO Series-Transducer Techniques, 0-100 mN, 0-1 N, and 0-10 N force ranges) so that the transmitted force may be recorded. A groove machined in the grip ensures axial alignment of the capillary and the load cell axis. The load cell is mounted to a combined translation/rotation stage (see Fig. 5a). A piezoelectric actuator (P-212 Series, Physik Instrumente, 0-60 μm and 0-120 μm actuation ranges) is secured to a second translation/rotation stage opposite from the load cell. The stages allow for precise alignment of the actuator and load cell to ensure that the direction of compression is aligned with the pillar axis. A silicon wafer fixed to the end of the actuator is used as a punch, which is treated with OTS to minimize friction and adhesion with the pillar face. The presence of friction at the punch/specimen interface has been shown to suppress shearing modes by confining the sample laterally.32-34 Determination of the in-pillar displacement ( $\Delta l = l_0 - l$ , where  $l_0$  is the initial pillar length and the sign convention is adopted to give positive values in compression) is made using the absolute displacement of the punch and the measured stiffness of each load cell.

The micropillars do not dry with a flat surface, and uneven contact between the punch and the pillar face results in large local stresses and crumbling at the pillar face. To minimize this effect, the pillar faces are formed prior to compression by extruding a small length of pillar ( $\sim 20~\mu m$  for a 580  $\mu m$  diameter pillar) and flattening the exposed pillar with the punch. Remnant particles are removed with compressed air, and the pillar is then extruded to the desired length.

The compression testing apparatus is positioned in the focal plane of an optical or laser scanning confocal microscope (reflectance mode,  $\lambda=639$  nm). The actuator is driven at a constant displacement rate between 0.1 and 1  $\mu m \ s^{-1}$  to a specified maximum displacement. The actuation direction is reversed to complete a full compression cycle. Force measurements are acquired throughout the cycle, which yields information about the loading and unloading stiffnesses and strengths of the pillars.

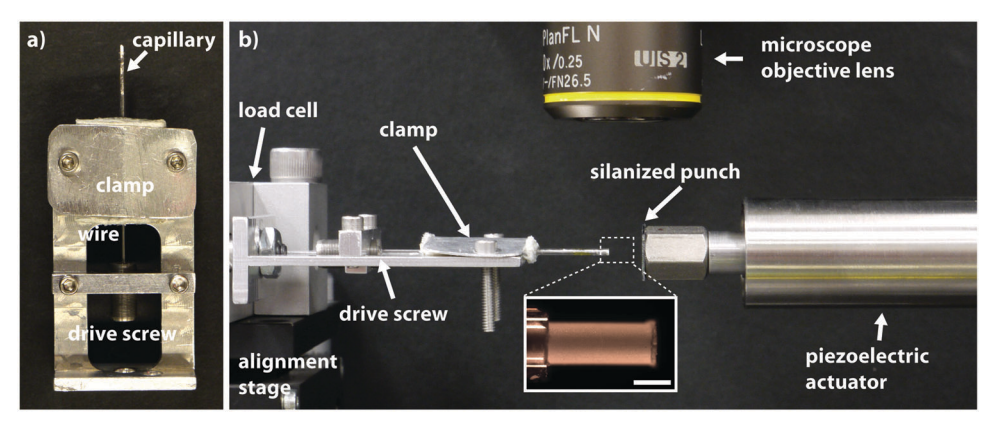


Fig. 5 (a) The custom grip. A wire with the same diameter as the capillary is used to push the pillar out of the capillary. A finely-threaded drive screw allows for precise control of the exposed pillar length. (b) Compression testing apparatus for colloidal micropillars. The capillary is secured to a custom grip using a clamp and the grip is fixed to a load cell. A displacement is generated using a silanized silicon punch attached to a piezoelectric actuator. The setup may be operated in the field-of-view of both optical and laser confocal microscopes to observe the pillar deformation during compression. Inset: an exposed pillar, scale bar 500 μm.

Digital images collected during compression allow for correlation of measurements of mechanical response with macroscopic events such as crack propagation or shear band propagation. Fluctuations in reflected intensity are visible for particles larger than  $\sim 5 \mu m$  at magnifications as low as 50×. These particles provide substantial natural image contrast that allows for the determination of surface displacement and strain from digital image correlation of a series of images. 35-37 Full-field strain maps of the pillar surface are calculated from the spatial gradients of the displacement fields. The image sequences also allow for the correlation of any pillar slip within the capillary tube to recorded load drops.

#### 3. Results and discussion

In situ micrographs and the mechanical response from a representative compression experiment of a 580 µm diameter pillar composed of 85 nm SiO<sub>2</sub> spheres are shown in Fig. 6. These pillars dry with a significant population of macroscopic cracks and the distribution of these defects governs deformation behavior. The force-displacement response may be partitioned into initial stiffening from  $\Delta l/l_o \approx 0$ –0.005, linear response from  $\Delta l/l_o \approx 0.005$ –0.010, and subsequent series of crack opening and propagation. Stiffening results from non-uniform contact between the pillar face and punch, which is mitigated in subsequent experiments by conditioning the pillar face according to the procedure outlined in Section 2.3. Therefore, the initial stiffening observed in this experiment should be regarded as an artifact of non-constant contact. Once the pillar-punch contact area becomes approximately constant, force increases linearly with  $\Delta l/l_0$ . No changes in the geometry of the cracks are observed during the stiffening and linear compression phases. The transition from linear to non-linear force response correlates with the opening of a crack near the punch face. During

opening, the crack separates along the direction of maximum tensile stress (perpendicular to the direction of compression) while the crack tip remains fixed. The crack remains stable (no observable tip movement) up to point b (normalized force,  $F/A_{o}$ , of 235 kPa where  $A_{o}$  is the cross-sectional area of the undeformed pillar), after which it propagates along a direction approximately parallel to the direction of compression. Crack propagation correlates with the first force drop at point c. The sequence of crack opening and propagation continues as  $\Delta l/l_o$ is increased further (see Fig. 6d and e). Interestingly, the peak force occurs after pre-existing cracks have propagated, presumably because of the deformation-induced densification of the heavily flawed pillar.

The behavior of a 580 µm diameter pillar composed of larger 250 nm SiO<sub>2</sub> spheres, which also forms with pre-existing macroscopic cracks, shows similar crack evolution during loading (see Fig. 7). The face of the pillar was conditioned prior to compression and thus no initial stiffening is observed. Linear force response is observed up to  $\Delta l/l_0 \approx 0.015$  after which a crack propagates down the pillar axis, resulting in a relatively large load drop. In contrast to the 85 nm SiO<sub>2</sub> pillar, no crack opening is observed prior to crack propagation, which occurs initially at a force of  $\sim 34$  mN (normalized force,  $F/A_0$ , of 123 kPa). The first active crack in the 250 nm SiO<sub>2</sub> pillar propagates the full length of the pillar axis. Therefore, the loadbearing ability of the pillar is greatly reduced, and subsequent displacement fails to produce forces more than  $\sim 1/2$  of that required to activate the first crack. By comparison, the first active crack in the 85 nm  $SiO_2$  pillar propagated  $\sim 1/2$  of the pillar length, and subsequent displacement generated forces larger than the force required to activate the first crack.

The compression experiments discussed are representative of the response observed in 12 85 nm pillars and 16 250 nm SiO<sub>2</sub> pillars. Collectively, we observe that the pillars composed

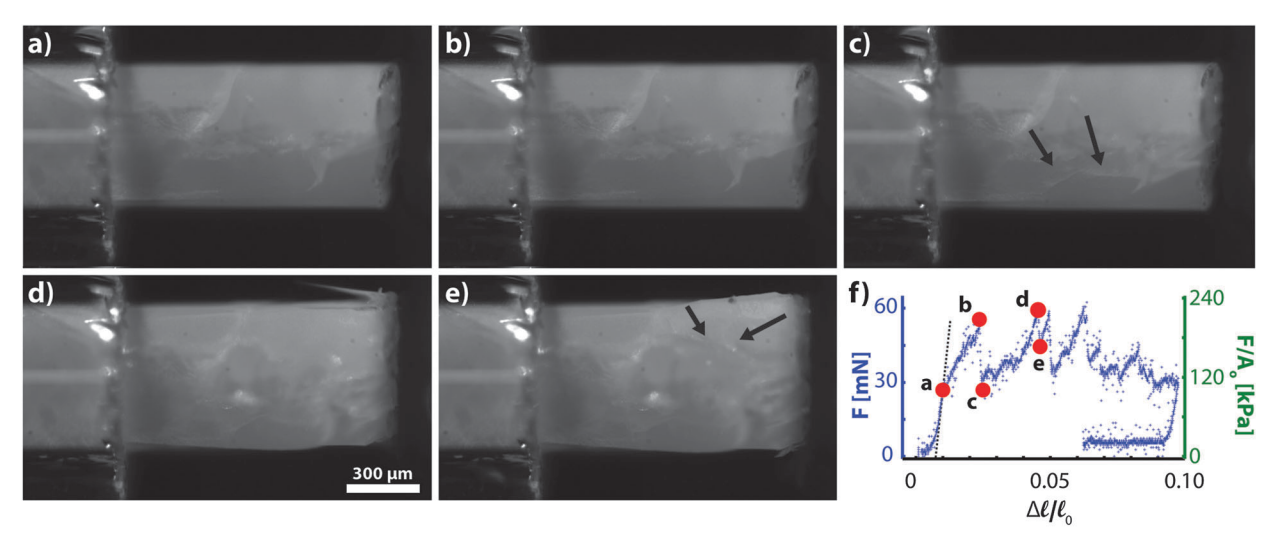


Fig. 6 A compression experiment on a  $580 \mu m$  diameter pillar composed of 85 nm SiO<sub>2</sub> spheres. The red dots in frame f correspond to the micrographs. The pillar behaves quasi-elastically (loading stiffness = 26.0 MPa, dashed line to denote linear response) up to point a, after which one of the cracks slowly opens (see frame b). The crack, highlighted by the black arrows in frame c, becomes unstable and propagates down the axis. This event corresponds to the first sudden load drop (see frame f). Subsequent loading opens and activates other cracks (frames d and e). The arrows in frame e indicate the crack corresponding to the load drop between frames d and e.

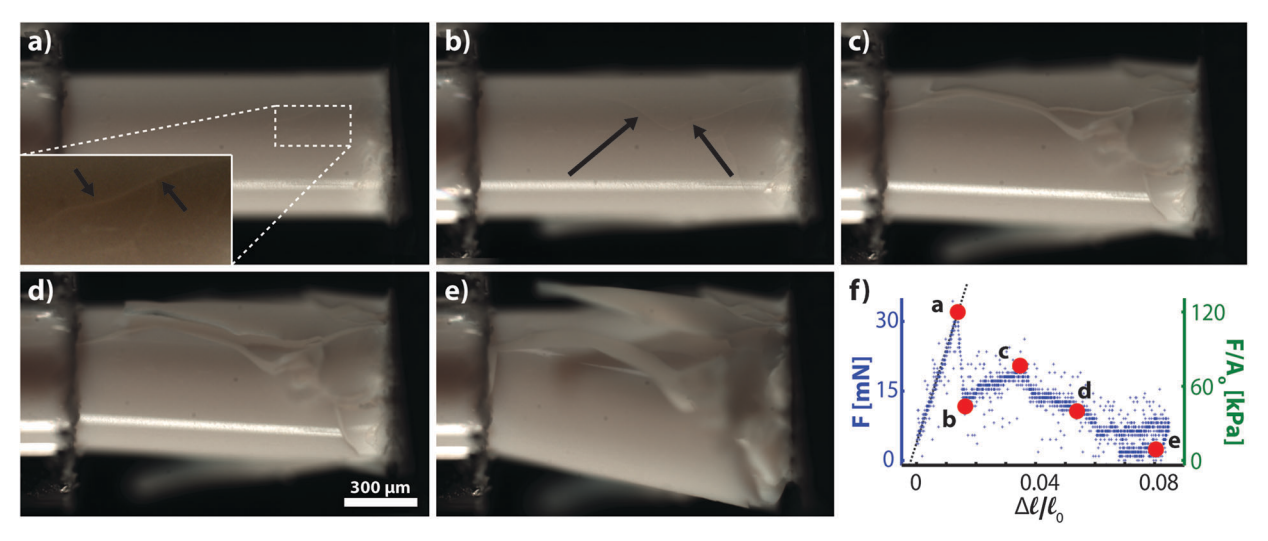


Fig. 7 A compression experiment on a 580 μm diameter pillar composed of 250 nm SiO<sub>2</sub> spheres. The red dots in frame f correspond to the micrographs. The pillar behaves quasi-elastically (loading stiffness = 7.1 MPa, dashed line to denote linear response) up to point a. A crack that formed during the drying process, highlighted by the arrows in frames a and b, becomes unstable during loading and propagates down the pillar axis (frame b). Subsequent loading opens this crack and activates other cracks (frames c, d and e).

of 85 nm and 250 nm SiO<sub>2</sub> dry with a large population of cracks, which ultimately dominate the mechanical response in comparison to the particle-level interactions. Similar to fracture processes observed in brittle solids, the yield force and peak force of our pre-cracked pillars are governed by the initial flaw population and its evolution during compression.<sup>38</sup> The force required for crack growth and propagation depends on the crack geometry (orientation and size) and particle-particle cohesion. While pillars with large populations of cracks are potentially interesting for fracture mechanics investigations, they are not suitable for probing shear banding behavior as the forces required to activate the cracks are less than the force required to nucleate shear bands. Thus, we next turn our attention to pillars synthesized with no apparent pre-existing flaws.

Pillars composed of a bidisperse mixture of 3/6 µm polystyrene spheres dry without cracking, and the deformation mode observed in these pillars is different from the crack opening/propagation found in pillars composed of smaller particles. As mentioned in Section 2.2, a bidisperse colloid size mixture is used to suppress crystallization and the resulting amorphous structure is confirmed from micrographs of the surface (Fig. 4). Micrographs and the mechanical response from a representative compression experiment of a 580  $\mu m$ diameter pillar composed of 3 and 6 µm polystyrene spheres are shown in Fig. 8.

Upon initial loading, force increases approximately linearly with  $\Delta l/l_0$  and the strain throughout the pillar is relatively uniform with only a slight enhancement of compressive strain near the punch (see Fig. 8a and b and 9a-d). As  $\Delta l/l_0$  increases, the magnitude of strain near the punch increases relative to the strain in the rest of the pillar. At a critical force of  $\sim 12.5$  mN (normalized force,  $F/A_0$ , of 47 kPa), the pillar begins to soften and each incremental displacement step results in a decrease in force. This softening corresponds to the nucleation of a shear

band near the punch face, as seen in Fig. 8c and d. During this nucleation stage, which persists from  $\Delta l/l_0 \approx 0.030-0.033$ , structural evolution is observable along the shear band region despite the absence of a clear shear offset at the pillar surface (see Movie S1, ESI†). Further displacement induces shear band propagation during which the pillar volumes separated by the shear band slip past one another and a detectable shear offset develops at the surface. Fig. 9 shows the evolution of the displacement and strain fields in the pillar. The heterogeneous strain field associated with the shear band is clearly visible in Fig. 9f. While the full orientation of the shear band is not determinable from the micrographs, it appears that the band forms along a direction approximately 45° from the direction of compression, which is parallel to the direction of maximum shear stress.

It is interesting to compare the deformation that we observe in the bidisperse 3/6 µm micropillars with the modes found in other amorphous systems. The shear bands that develop in the micropillars have a finite thickness. From inspection of micrographs acquired during shear band propagation, we estimate the thickness to be  $\sim 5$  particle diameters (see Movie S1 in ESI†). This thickness is consistent with the values reported in a sheared suspension of colloidal PMMA particles.<sup>39</sup> The shear band orientation of approximately 45° from the direction of compression is similar to the angle observed in experiments<sup>40</sup> and simulations<sup>41</sup> of compression of other granular solids. The examination of deviations from this angle has been suggested as a method to gain insight on the pressure dependence of yielding in disordered solids, 14 which is a venue for future work. The available degrees of freedom in the current testing apparatus do not provide the resolution necessary to precisely measure this angle. Nevertheless, we consistently observe shear bands that originate at the micropillar/punch interface and grow to intersect a free surface. Without the confining walls

**PCCP** Paper

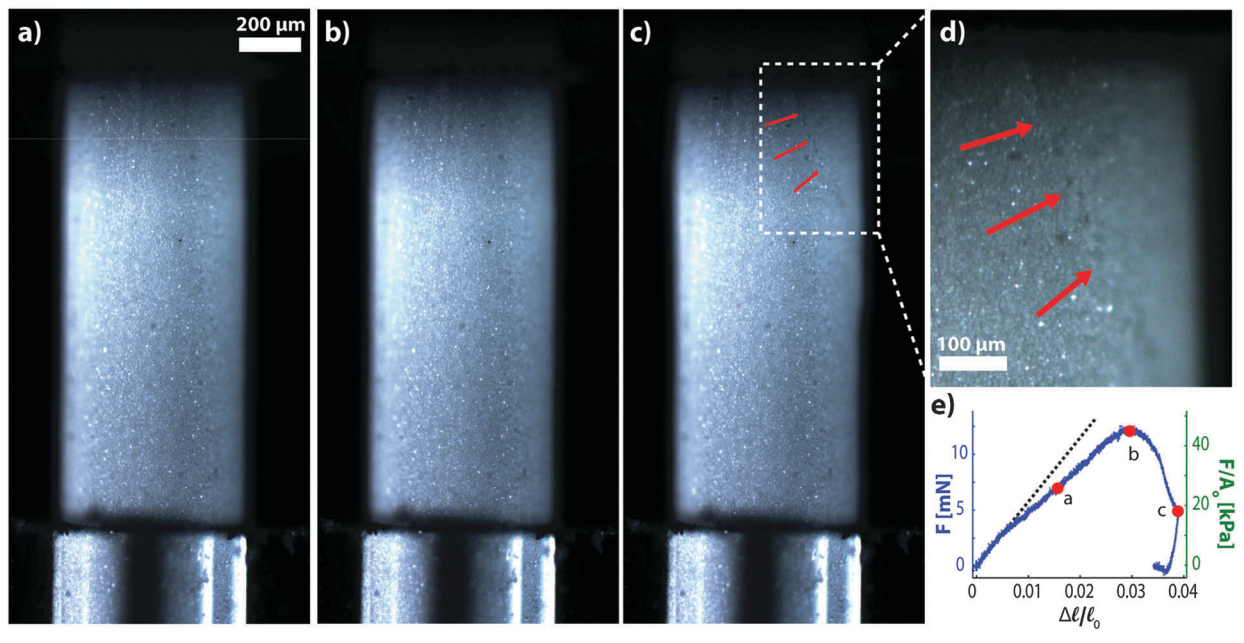


Fig. 8 Optical micrographs acquired during compression of a 580 μm diameter pillar composed of 3 and 6 μm polystyrene spheres. The punch is located at the top face of the pillar and actuates downward. The inset at the lower right shows the mechanical response (loading stiffness = 2.3 MPa, dashed line to denote linear response). At the point marked b, a shear band begins to form. The mature shear band is indicated in frames c and d.

found in other granular compression experiments, there is no restoring force for radial displacements. Therefore, local softening due to dilatory structural evolution is concentrated near the punch and results in the preferential location for shear band formation. This behavior more closely resembles that found in compression experiments of micro-scale BMG pillars. 42-44

Although the orientation and location of the shear bands are consistent from pillar to pillar, the normalized force at shear banding onset,  $F/A_0$  is found to vary from 47 to 830 kPa. While intrinsic structural variation from pillar to pillar surely affects the response, we believe that fluctuating humidity accounts for much of the variability. All of the experiments reported to this point were performed in ambient conditions with no special provisions taken to control humidity levels. To explore the effect of humidity on pillar response, an environmental chamber capable of varying relative humidity (RH) from <2% RH to >98% RH was constructed for the compression testing apparatus.

Multiple compressions of a single micropillar at various levels of RH illustrate the impact of environmental conditions on the mechanical response. A 900 µm diameter pillar composed of 3/6 µm PS spheres is compressed 25 times to displacements much less than the values necessary to cause shear banding ( $\Delta l/l_0 < 0.003$ ). Over the course of the compressions, RH is adjusted from near saturation (96% RH) to dry (<2% RH) and then back to near saturation. Eight of the response curves are plotted in Fig. 10a. The plot ordering follows the sequence of testing, with the left-most plot corresponding to the first compression and the right-most plot corresponding to the last compression. Blue, red, green, and black plots correspond to 96% RH, 51% RH, 21% RH, and <2% RH environments, respectively. It is found that decreasing RH results in significant stiffening of the pillar, and

subsequent increasing of RH restores the compliance of the pillar. To quantify the variation, polynomials are fit to the load and unload responses, expressed as  $F/A_0$  vs.  $\Delta l/l_0$ , for each of the 25 compression experiments (see fitting procedure in ESI†). The maximum instantaneous stiffness, as determined from the maximum value of  $\frac{l_{\rm o}}{A_{\rm o}}\frac{{\rm d}F}{{\rm d}\Delta l}$  over the range of  $\Delta l/l_{\rm o}$ , is extracted for each compression. Fig. 10b plots the maximum instantaneous load and unload stiffnesses for different values of RH. A low RH environment results in a pillar that is 10× stiffer than the same pillar compressed in a high RH environment. The decrease in unload stiffness with increasing RH is non-monotonic and reaches a maximum between 35-50% RH, where we observe a two-fold increase in the unload stiffness over the stiffness at <2% RH. The magnitude of the stiffness increase is similar to that observed in a colloidal crystal indented at various levels of RH. 45 The cross-over region between the extreme values of stiffness extends over a wide range of RH (~30-70% RH) that overlaps with typical ambient RH variation.

Increasing environmental RH increases the moisture content in the pillar due to capillary condensation. In the limit of a completely dry pillar, a state not realizable in our system, particle-particle cohesion due to water-bridges vanishes. At low RH, water-bridges form at the contact points between particles and increase cohesion. When these water-bridges remain distinct, the pillar is said to be in the pendular state<sup>46</sup> defined for wet granular media. Increasing RH further results in some of the water-bridges merging and completely filling some of the voids in the pillar. The pillar is said to be in the funicular state. Higher RH may saturate the pillar and fill all of the voids and the pillar is said to be in the capillary state.

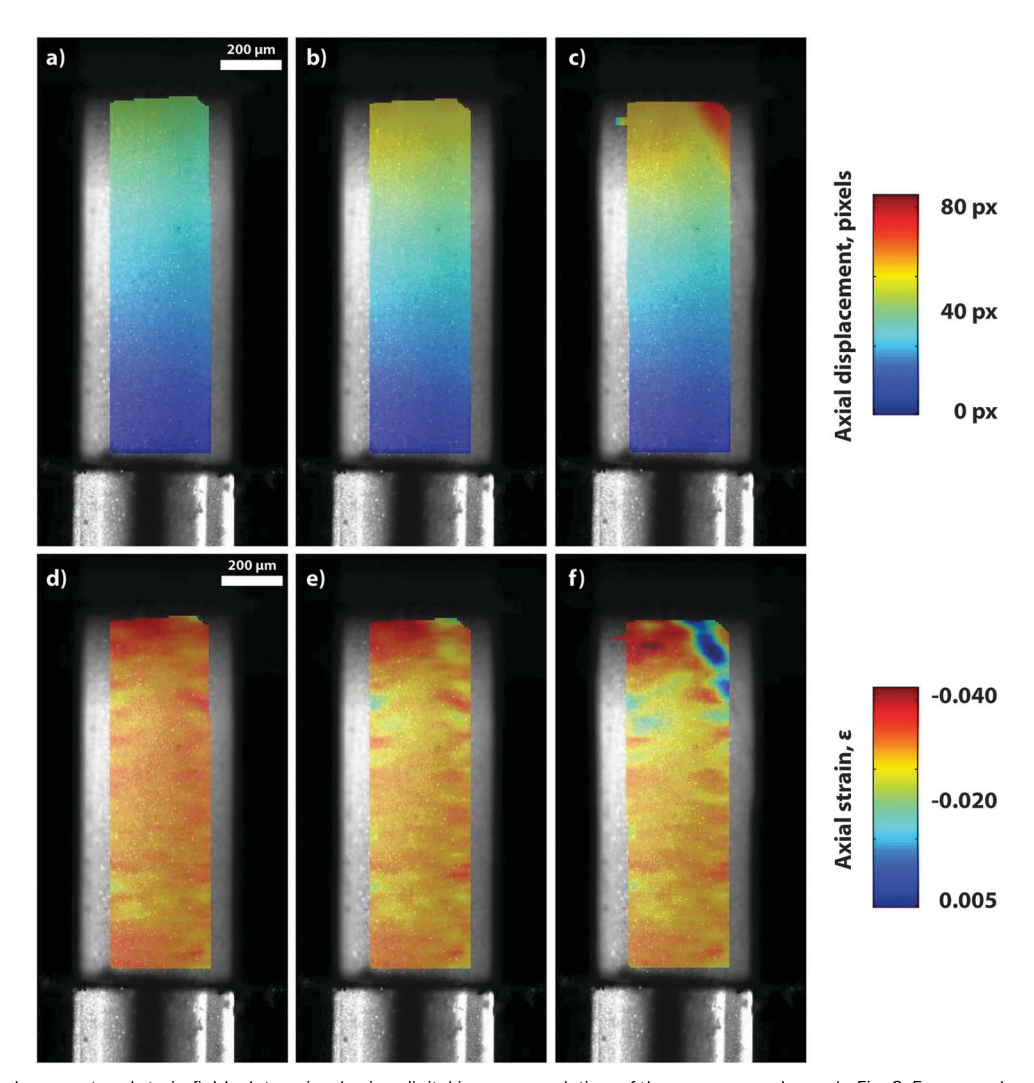


Fig. 9 In-pillar displacement and strain fields determined using digital image correlation of the sequences shown in Fig. 8. Frames a, b, and c show the axial displacement at the points marked a, b, and c in Fig. 8e, respectively. Frames d, e, and f show the axial strain at points a, b, and c in Fig. 8e, respectively.

Dynamic vapor sorption (DVS) is performed to quantify the water content in the pillar as a function of RH. DVS employs a precision microbalance to measure the change in the mass of a sample with changes in RH. The relative change in mass of the pillar is given by  $m(RH)/m_{dry}$  where  $m_{dry}$  is the mass of the dry pillar and m(RH) is the mass of the pillar at a given RH. The bulk volume,  $V_{\text{bulk}}$ , of the pillar is determined using optical microscopy and the void volume,  $V_{\text{void}}$ , is determined through the relation:

$$V_{\mathrm{void}} = V_{\mathrm{bulk}} - \frac{m_{\mathrm{dry}}}{\rho_{\mathrm{PS}}}$$

where  $\rho_{PS}$  is the density of PS (1.06 g cc<sup>-1</sup>). For the 900  $\mu m$ diameter pillar composed of 3/6  $\mu$ m PS spheres,  $V_{\text{void}}/V_{\text{bulk}} = 0.24$ . The water content in the pillar is quantified in the dimensionless water content:

$$\frac{V_{\text{water}}}{V_{\text{void}}} = \frac{\left[m(\text{RH}) - m_{\text{dry}}\right]}{\rho_{\text{H}_2\text{O}} \times V_{\text{void}}}$$

where  $\rho_{\rm H,O}$  is the density of water (1.00 g cc<sup>-1</sup>). The relative change in mass and RH during a DVS experiment are plotted against time in Fig. 11a, and the equilibrium relative change in mass and water content are plotted against RH in Fig. 11b. It is found that the relationship between water content and RH is not linear, with a sharp increase in water content for RH values > 80%.

Particle-particle cohesion and friction are markedly different in the pendular, funicular, and capillary states, 46 and these variations are reflected in the distinct mechanical responses observed at different RH. In the pendular state, where  $0 < V_{\text{water}}/V_{\text{void}} < 0.10-0.25,^{40}$  cohesive forces are the result of water-bridges that form between particles. In the capillary state, where  $V_{\text{water}}/V_{\text{void}} > 0.90$ , cohesion is the result of suction generated in the fluid phase containing the particles. Cohesion in the funicular state is a combination of the cohesive interactions characteristic of the pendular and capillary states. Friction is greatly reduced in the capillary state in which the large water content serves as a lubricant between particles. In comparing the compression data with water content, we see that the maximum unloading stiffness achieved at 50% RH corresponds to a water content of  $\sim 0.12-0.15$ , a value associated with the pendular regime. Increasing RH beyond

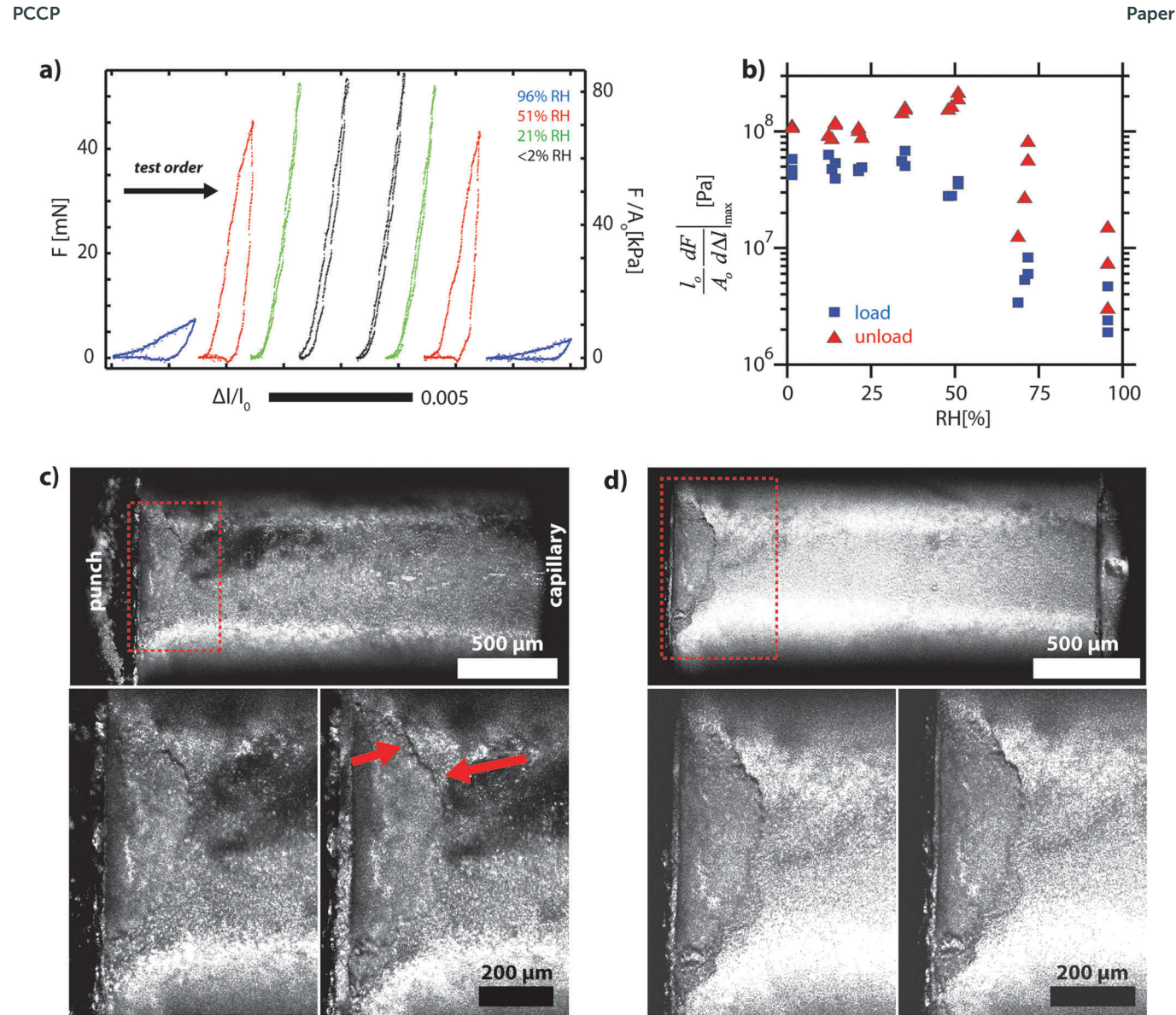


Fig. 10 (a) Eight sequential response curves for a pillar compressed at different RH. (b) The variation of the maximum instantaneous stiffness on load and unload with changes in RH. (c) Confocal micrographs from a pillar compressed at 96% RH. Top frame shows entire pillar, lower left frame shows region denoted by red box prior to compression, and the lower right frame shows the same region after compression. Significant structural evolution of a previously sheared region is observed. (d) Confocal micrographs from a pillar compressed at <2% RH. Top frame shows entire pillar, lower left frame shows region denoted by red box prior to compression, and the lower right frame shows the same region after compression. Little structural evolution of a previously sheared region is observed.

50% results in a significant decrease in the loading and unloading stiffnesses which we attribute to increased plasticity. We quantify the extent of plasticity at a given RH through two metrics: efficiency,  $\eta$ , and the ratio of the maximum instantaneous stiffness on unload to the maximum instantaneous stiffness on load. We define  $\eta$  as the ratio of the work done by the system on unloading to the work done on the system during loading:

$$\eta = \frac{\int_{x_{\text{max}}}^{0} F_{\text{unload}}(x') dx'}{\int_{0}^{x_{\text{max}}} F_{\text{load}}(x') dx'}$$

An efficiency of 1 would indicate a perfectly elastic process and an efficiency of 0 would indicate a perfectly plastic, or dissipative, process. The efficiency of the compression cycles as a function of RH is plotted in Fig. 11c. At low RH,  $\eta \approx 0.8$ , which is the maximum value observed. At RH > 30%,  $\eta$  drops significantly and settles to values  $\approx 0$  at 70% RH. Near saturation, several negative efficiency values are measured, indicating that the net work done on the pillar during unloading is positive (i.e., energy is put into the system on unloading). We attribute this effect to strong adhesion between the pillar face and the punch; pulling the pillar face off of the punch involves breaking many water-bridges that form between the surfaces during compression, which requires energy. The precipitous drop in  $\eta$  at RH values above 30% is indicative of significantly increased plasticity that occurs through dissipative mechanisms like particle sliding and rolling. This assertion is reinforced by the drastic increase in the ratio of the maximum instantaneous

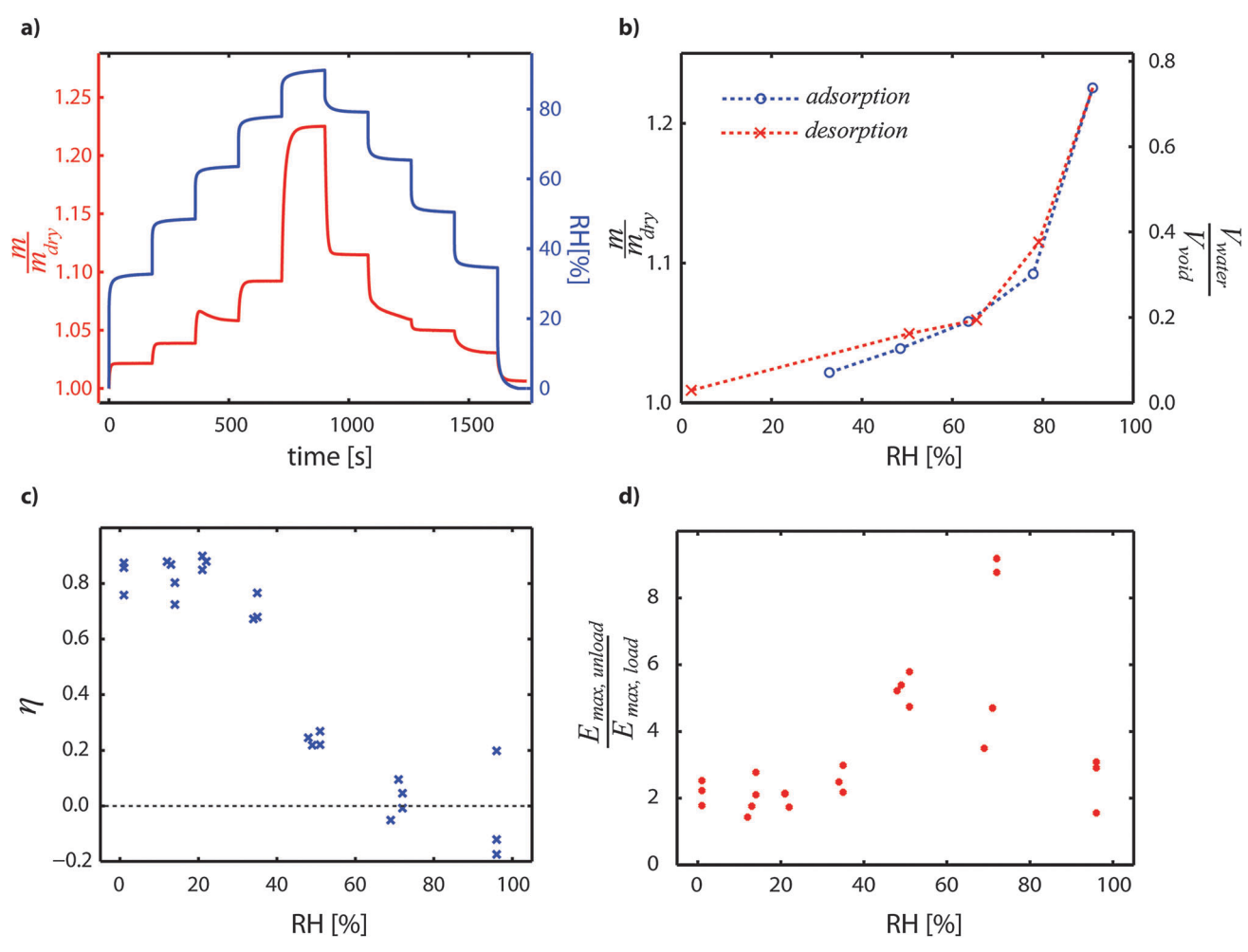


Fig. 11 (a) The relative change in mass and RH plotted against time for a 900 µm diameter pillar composed of 3/6 µm PS spheres. (b) The equilibrium relative change in mass and water content as a function of RH on adsorption and desorption. (c) The efficiency, a measure of the work recovered during a compression cycle, as a function of RH. (d) The ratio of the maximum instantaneous stiffness on unload,  $E_{\text{max,unload}}$ , to the maximum instantaneous stiffness on loading,  $E_{\rm max,load}$ 

stiffness on unload to the maximum instantaneous stiffness on load,  $E_{
m max,unload}/E_{
m max,load}$ , which increases from  $\sim 2$  at RH <40% to values between 4 and 9 at 40% < RH < 70%, corresponding to water content values  $\sim 0.16-0.22$ . Taken as a whole, the water content and stiffness data indicate maximum cohesion at 50% RH and increased plasticity at >30% RH.

Confocal micrographs of a single pillar compressed to larger values of  $\Delta l/l_0$  show a fundamental change in deformation in two extreme RH environments (see Fig. 10c and d). In Fig. 10c and d, the top image is the pillar prior to compression, the lower left image is the region outlined by the dashed red-box prior to compression, and the lower right image is the same region after compression. At 96% RH (Fig. 10c), significant evolution of a previously sheared region (indicated by the red arrows) is observed during compression. Conversely, the sheared region in the very dry (<2% RH, Fig. 10d) pillar shows little evolution.

The effect of varying levels of cohesion and friction on shear band nucleation and propagation is not clear. However, we have shown that the macroscopic quasi-elastic response of our pillars is a strong function of RH. The strong correlation

between water content within the pillars, and measurements of mechanical stiffness and efficiency suggest that RH strongly affects particle-particle cohesion and friction. In BMGs, a high ratio of the bulk modulus, B, to the shear modulus, G, has been associated with increased fracture toughness and plasticity.<sup>47</sup> This relationship has been rationalized by equating a high B with the suppression of dilation and a low shear modulus with lower resistance to plastic flow. Therefore, large B/G promotes more shear band operation prior to final fracture. Exploring the effect of varying macroscopic elastic properties in our model micropillar packings, which can be widely controlled via tunable particle interactions, on plasticity and fracture may guide refinement of predictive models for design of tough atomic solids.

### Conclusion and outlook

We have shown a novel synthetic approach for producing freestanding disordered colloidal pillars with tailored particle and pillar sizes and tunable particle-particle interactions. Through

quantitative in situ uniaxial compression, we demonstrate that colloidal pillars are a promising model system for probing plasticity and finite size effects in amorphous solids owing to the strong cohesive interactions unique to the micrometer and submicrometer scale particles. Whereas pillars composed of submicrometer scale particles show stochastic response that is dictated by the inherent population of macroscopic cracks, plasticity in pillars composed of a bidisperse mixture of micrometer scale particles is governed by shear banding. We find that the characteristics of shear banding in our disordered pillars show remarkable similarity to those observed in metallic glasses, supporting the applicability of colloidal packings as a model system for atomic glasses. We furthermore show that control of relative humidity levels during compressive testing leads to distinct mechanical response, which we attribute to varying cohesion and friction between contacting particles. The combination of tunable interactions, control of fundamental length scales through capillary and particle size control, quantitative mechanical testing, and direct visualization at the particle level provides a unique platform for elucidating new insight on the dynamics and plasticity mechanisms of disordered solids. We envisage the information gained from such studies to inform the synthesis of new designer materials with enhanced toughness and damage tolerance coupled with more graceful failure.

## Acknowledgements

We gratefully acknowledge financial support from the National Science Foundation through PENN MRSEC DMR-1120901. We thank the Penn Nanoscale Characterization Facility for technical support. We thank Prof. Yossef Elabd and Jacob Nykaza of Drexel University for their assistance with the DVS experiments. We also thank J. Senese for his assistance in constructing the environmental chamber.

#### References

- L. Bragg and J. F. Nye, Proc. R. Soc. London, Ser. A, 1947, 190, 474–481.
- 2 L. Bragg, J. Sci. Instrum., 1942, 19, 148.
- 3 P. Schall, D. A. Weitz and F. Spaepen, *Science*, 2007, **318**, 1895–1899.
- 4 A. Dinsmore, E. Weeks, V. Prasad, A. Levitt and D. A. Weitz, *Appl. Opt.*, 2001, **40**, 4152–4159.
- 5 Y. Rahmani, K. van der Vaart, B. van Dam, Z. Hu, V. Chikkadi and P. Schall, *Soft Matter*, 2012, **8**, 4264–4270.
- 6 V. Chikkadi and P. Schall, *Phys. Rev. E: Stat., Nonlinear, Soft Matter Phys.*, 2012, **85**, 031402.
- 7 P. Schall, I. Cohen, D. A. Weitz and F. Spaepen, *Nature*, 2006, 440, 319–323.
- 8 D. Mueth, G. Debregeas, P. Karczmar, S. Nagel and H. Jaeger, *Nature*, 2000, **406**, 385–389.
- 9 T. Aste, M. Saadatfar and T. J. Senden, *Phys. Rev. E: Stat.*, *Nonlinear, Soft Matter Phys.*, 2005, **71**, 061302.

- 10 M. Scheel, R. Seemann, M. Brinkmann, M. Di Michiel, A. Sheppard, B. Breidenbach and S. Herminghaus, *Nat. Mater.*, 2008, 7, 189–193.
- 11 A. Yethiraj and A. van Blaaderen, *Nature*, 2003, **421**, 513–517.
- 12 K. Frye and C. Marone, *J. Geophys. Res.: Solid Earth*, 2002, **107**, ETG 11-1-ETG 11-13.
- 13 M. L. Falk and J. S. Langer, *Phys. Rev. E: Stat. Phys., Plasmas, Fluids, Relat. Interdiscip. Top.*, 1998, 57, 7192–7205.
- 14 C. A. Schuh, T. C. Hufnagel and U. Ramamurty, *Acta Mater.*, 2007, 55, 4067–4109.
- 15 L. Zhang, G. Feng, Z. Zeravcic, T. Brugarolas, A. J. Liu and D. Lee, ACS Nano, 2013, 7, 8043–8050.
- 16 A. S. Argon and H. Y. Kuo, *Mater. Sci. Eng.*, 1979, 39, 101–109
- 17 J. Desrues and R. Chambon, *Int. J. Solids Struct.*, 2002, **39**, 3757–3776.
- 18 A. S. Argon, Acta Metall., 1979, 27, 47-58.
- 19 M. L. Falk and J. S. Langer, *Annu. Rev. Condens. Matter Phys.*, 2011, 2, 353-373.
- 20 E. Bouchbinder, J. S. Langer and I. Procaccia, *Phys. Rev. E: Stat., Nonlinear, Soft Matter Phys.*, 2007, 75, 036107.
- 21 P. Y. Huang, S. Kurasch, J. S. Alden, A. Shekhawat, A. A. Alemi, P. L. McEuen, J. P. Sethna, U. Kaiser and D. A. Muller, *Science*, 2013, 342, 224–227.
- 22 H. Guo, P. F. Yan, Y. B. Wang, J. Tan, Z. F. Zhang, M. K. Sui and E. Ma, *Nat. Mater.*, 2007, **6**, 735–739.
- 23 C. A. Volkert, A. Donohue and F. Spaepen, J. Appl. Phys., 2008, 103, 083539.
- 24 F. Soulié, F. Cherblanc, M. S. El Youssoufi and C. Saix, *Int. J. Numer. Anal. Methods Geomech.*, 2006, **30**, 213–228.
- 25 V. Richefeu, M. S. El Youssoufi and F. Radjaï, *Phys. Rev. E: Stat., Nonlinear, Soft Matter Phys.*, 2006, **73**, 051304.
- 26 S. H. Nguyen, A. Chemenda and J. Ambre, *Int. J. Rock Mech. Min.*, 2011, **48**, 103–115.
- 27 Y. Rahmani, R. Koopman, D. Denisov and P. Schall, *Sci. Rep.*, 2013, 3, 1064.
- 28 N. Keim and P. Arratia, Phys. Rev. Lett., 2014, 112, 028302.
- 29 M. S. Tirumkudulu and W. B. Russel, *Langmuir*, 2005, 21, 4938–4948.
- 30 K. Singh and M. Tirumkudulu, Phys. Rev. Lett., 2007, 98, 1-4.
- 31 A. Kansal, S. Torquato and F. Stillinger, *J. Chem. Phys.*, 2002, **117**, 8212–8218.
- 32 H. A. Kuhn, *ASM Handbook, Materials Testing and Evaluation*, 2000, vol. 8, p. 338.
- 33 F. F. Wu, Z. F. Zhang and S. X. Mao, *J. Mater. Res.*, 2007, 22, 501–507.
- 34 A. L. Greer, Y. Q. Cheng and E. Ma, *Mater. Sci. Eng.*, *R*, 2013, 74, 71–132.
- 35 M. Sutton, J. Orteu and H. Schreier, *Image Correlation for Shape, Motion and Deformation Measurements: Basic Concepts, Theory and Applications*, 2009, p. 322.
- 36 C. Eberl, D. S. Gianola and K. J. Hemker, *Exp. Mech.*, 2012, **50**, 85–97.
- 37 C. Eberl, R. Thompson, D. S. Gianola, W. Sharpe Jr. and K. J. Hemker, "Digital image correlation and tracking",

- MATLAB file exchange, http://www.mathworks.com/matlab central/fileexchange/12413-digital-image-correlation-and-tracking, 2006.
- 38 M. F. Ashby and S. D. Hallam, Acta Metall., 1986, 34, 497-510.
- 39 L. Isa, R. Besseling and W. C. K. Poon, *Phys. Rev. Lett.*, 2007, **98**, 198305.
- 40 A. Rechenmacher, J. Mech. Phys. Solids, 2006, 54, 22-45.
- 41 K. Iwashita and M. Oda, Powder Technol., 2000, 109, 192-205.
- 42 A. Dubach, R. Raghayan, J. F. Löffler, J. Michler and U. Ramamurty, *Scr. Mater.*, 2009, **60**, 567–570.
- 43 C. J. Lee, J. C. Huang and T. G. Nieh, *Appl. Phys. Lett.*, 2007, **91**, 161913.
- 44 Y. H. Lai, C. J. Lee, Y. T. Cheng, H. S. Chou, H. M. Chen, X. H. Du, C. I. Chang, J. C. Huang, S. R. Jian, J. S. C. Jang and T. G. Nieh, *Scr. Mater.*, 2008, 58, 890–893.
- 45 F. Gallego-Gómez, V. Morales-Florez, Á. Blanco, N. de la Rosa-Fox and C. López, *Nano Lett.*, 2012, 12, 4920–4924.
- 46 N. Mitaraia and F. Nori, Adv. Phys., 2006, 55, 1-45.
- 47 J. J. Schroers and W. L. Johnson, *Phys. Rev. Lett.*, 2004, 93, 255506.